

Higher Landau-Level Analogues and Signatures of Non-Abelian States in Twisted Bilayer MoTe₂

Chong Wang,^{1,*} Xiao-Wei Zhang,^{1,*} Xiaoyu Liu,¹ Jie Wang,² Ting Cao,^{1,†} and Di Xiao^{1,3,‡}

¹*Department of Materials Science and Engineering, University of Washington, Seattle, WA 98195, USA*

²*Department of Physics, Temple University, Philadelphia, Pennsylvania, 19122, USA*

³*Department of Physics, University of Washington, Seattle, WA 98195, USA*

Recent experimental discovery of fractional Chern insulators at zero magnetic field in moiré superlattices has sparked intense interests in bringing Landau level physics to flat Chern bands. In twisted MoTe₂ bilayers (tMoTe₂), recent theoretical and experimental studies have found three consecutive flat Chern bands at twist angle $\sim 2^\circ$. In this work, we investigate whether higher Landau level physics can be found in these consecutive Chern bands. At twist angles 2.00° and 1.89° , we identify four consecutive $C = 1$ bands for the K valley in tMoTe₂. By constructing Wannier functions directly from density functional theory (DFT) calculations, a six-orbital model is developed to describe the consecutive Chern bands, with the orbitals forming a honeycomb lattice. Exact diagonalization on top of Hartree-Fock calculations are carried out with the Wannier functions. Especially, when the second moiré miniband is half-filled, signatures of non-Abelian states are found. Our Wannier-based approach in modelling moiré superlattices is faithful to DFT wave functions and can serve as benchmarks for continuum models. The possibility of realizing non-Abelian anyons at zero magnetic field also opens up a new pathway for fault-tolerant quantum information processing.

Introduction.—Recent experiments [1–5] and theories [6–12] have identified a series of Abelian fractional Chern insulators (FCI), such as the Laughlin states and other Jain sequence states, as well as gapless composite fermi liquids (CFL), in moiré superlattices at zero magnetic field. The emergence of these exotic states is attributed to the existence of flat Chern bands [13–16] in these systems. Specifically, in twisted homobilayer transition metal dichalcogenides (TMD), within the framework of the continuum model, electrons can be viewed as hopping in a layer pseudospin skyrmion lattice, giving rise to topologically nontrivial flat bands [17, 18]. The quantum geometry of these flat Chern bands resembling that of the lowest Landau level is one of the important reasons for the emergence of the above exotic states [19–26].

More exotic states, such as the Moore-Read (MR) state featuring non-Abelian excitations [27], can be stabilized by Coulomb interaction in the first LL [28–31]. In a recent density functional theory (DFT) study of twisted bilayer MoTe₂ (tMoTe₂), it is discovered that three consecutive flat bands with Chern numbers equal to 1 appear at twist angle 2.14° for each valley [32], which has not been predicted in the continuum model description within the first harmonic approximation. The existence of three consecutive flat Chern bands has also been corroborated by experimental observations at similar twist angles [33]. These consecutive flat Chern bands with identical Chern numbers bear a striking resemblance to the series of Landau levels, hinting at the possibility of bring higher Landau level physics to moiré superlattices at zero magnetic field, especially the non-Abelian state such as MR.

In this work, we first extend our previous large-scale DFT calculations on tMoTe₂ to additional twist angles near 2° . We identify four consecutive $C = 1$ bands at twist angles 2.00° and 1.89° for the K valley. To accurately describe the

band geometry, we construct Wannier functions directly from DFT calculations and develop a six-orbital model to describe the consecutive Chern bands, where the orbitals form a honeycomb lattice. For the second moiré miniband, the integral of the trace of the Fubini-Study metric [$\text{tr}(g)$] is shown to be close to that of the first Landau level. In addition, the fluctuations of Berry curvature and $\text{tr}(g)$ can be significantly suppressed by band mixing in Hartree-Fock (HF) calculations, enhancing the analogy between the second moiré miniband and the first Landau level. Exact diagonalization (ED) on top of HF calculations are carried out using the Wannier functions. When the second moiré miniband is half-filled, signatures of non-Abelian states are found. Our Wannier-based approach in modelling the moiré superlattice is faithful to DFT wave functions and can serve as benchmarks for continuum models. The possibility of realizing non-Abelian states in tMoTe₂ also opens up an exciting avenue in realizing higher LL physics in moiré superlattices.

Consecutive Chern bands in tMoTe₂.—When moiré superlattices are formed by twisting two identical monolayers, the original monolayer bands are broken into minibands. For monolayer MoTe₂, the valence band top is located at two corners (K and K') of the honeycomb Brillouin zone. In moiré superlattices, the bands from both K and K' valley form two independent sets of minibands. The two sets of bands are partners under the operation of time reversal symmetry. Our previous large-scale density-functional-theory (DFT) calculations with machine learning force fields has revealed an intricate dependence of the band topology on twist angles [32]. Interestingly, at twist angle of 2.14° , K valley valence bands of tMoTe₂ feature three consecutive Chern bands with $C = 1$. With hole doping, these Chern bands can be revealed in experiments when valleys are spontaneously polarized due to electron-

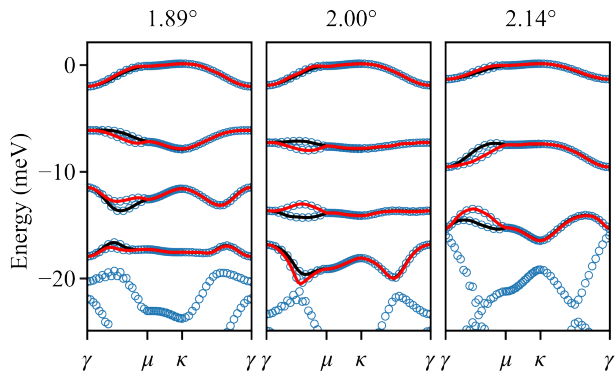


FIG. 1. Bands for tMoTe₂ at twist angles 1.89°, 2.00° and 2.14°. Empty blue circles are from DFT calculations, and solid lines are from Wannier interpolation. For Wannier interpolated bands, red lines are from the K (spin up) valley and black lines are from the K' (spin down) valley. All Wannier interpolated bands have Chern number $C = +1$ for the K valley. Only Wannier interpolated bands in the frozen window are shown here.

electron interactions.

To further explore the band topology of tMoTe₂ around this twist angle, we have performed DFT calculations at two other twist angles 2.00° and 1.89°, following the same method introduced in Ref. [32]. The moiré valence bands from all three angles are shown in Fig. 1. Four consecutive $C = 1$ bands from K valley are found at twist angles 2.00° and 1.89°. At twist angle 2.14°, the fourth band is not well-isolated to have a well-defined Chern number. The Chern numbers are determined by Wannier interpolation with Wannier functions, whose construction will be described below.

The consecutive Chern bands are flat, hinting at the possibility of strong-correlated physics when these bands are partially filled. In this work, we focus on the possibility of realizing first Landau level physics in tMoTe₂, specifically targeting the second valence band (bands are numbered in the descending order of energy). At the twist angle 2.00°, the second valence band reaches optimal flatness. Therefore, we will focus on this twist angle in the following, deferring the results from other twist angles to Supplemental Material.

Band geometry from Wannier functions.—To investigate whether consecutive moiré valence bands resemble LL series, accurate modelling is required to capture fluctuations of band geometry. Currently, the most common description of moiré superlattice is continuum models, in which the effect of moiré superlattice is described by moiré potentials periodic in the moiré Bravais lattice vectors. However, continuum models fitted to DFT bands within the first few harmonic moiré potentials do not guarantee an accurate reproduction of the band geometry such as the Berry curvature Ω and the Fubini-Study metric g from DFT wave functions. Here, we construct Wannier functions to faithfully represent DFT wave functions and perform many-body calculations on top of the Wannier functions. The Wannier

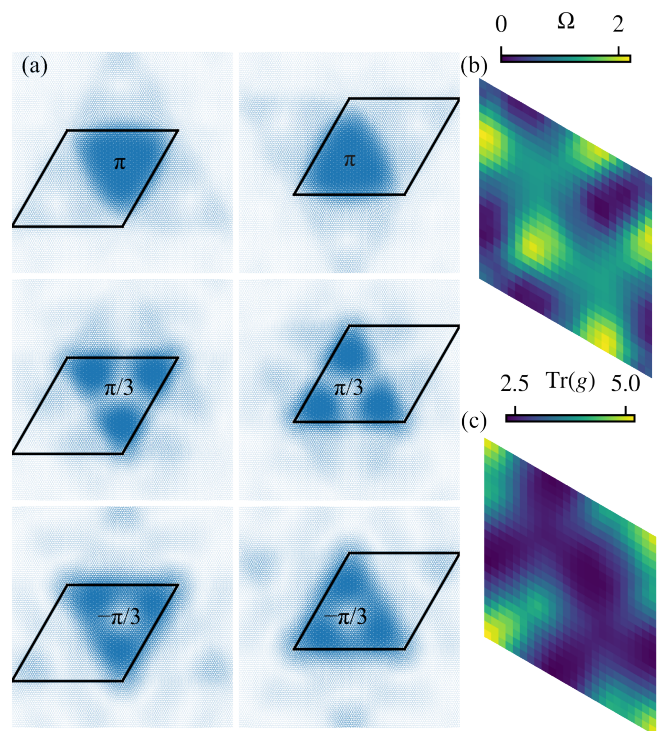


FIG. 2. (a) Real space distributions of the Wannier functions for tMoTe₂ at twist angle 2.00°. Black parallelograms represent moiré unit cell. C_3 eigenvalues with respect to the center of the Wannier functions have been labeled (C_3 eigenvalues take the form of $e^{i\alpha}$, and α is labelled in the figure). Contribution from both layers have been summed over. (b) and (c) show the distribution of the Berry curvature Ω and the trace of the Fubini-Study metric $\text{tr}(g)$ in the Brillouin zone for the second moiré miniband. The unit for both Ω and $\text{tr}(g)$ is $2\pi/|\Gamma|$, where $|\Gamma|$ is the area of the Brillouin zone. Both Ω and $\text{tr}(g)$ are calculated from the small- \mathbf{q} expansion of the form factors.

functions are constructed for the K valley bands, and the K' valley Wannier functions are obtained using time reversal symmetry. The valleys in the DFT calculations are decoupled by distinct Bloch phases and opposite expectation values of the spin- z operator.

Our approach to construct the Wannier functions is the “projection” method [34], which is also the first step in constructing maximally localized Wannier functions [35, 36]. This approach first chooses several trial Wannier functions and project the relevant Bloch states onto the trial Wannier functions. The projected Bloch states are subsequently orthogonalized. The Fourier transformation of the orthogonalized projected Bloch states gives the desired Wannier functions. This method generally retains the symmetry properties of the trial Wannier functions [36] and is a powerful tool to construct tight-binding models from DFT calculations.

The DFT band structure does not possess a local gap above which the total Chern number is zero. Therefore, band disentanglement [37] needs to be performed to avoid Wannier obstruction [38]. A set of frozen states is chosen

for which the DFT band energies and Bloch states are faithfully reconstructed. For twist angle 2.14° , we choose the first three valence bands as frozen states. For twist angles 2.00° and 1.89° , first four bands are frozen.

For twist angle 2.00° , the real space plots of the Wannier functions are shown in Fig. 2(a). The Wannier functions form a honeycomb lattice. For each site in the honeycomb lattice, there are three Wannier functions with different C_3 symmetry eigenvalues. Together they form a six-orbital honeycomb model. We have chosen trial Wannier functions centered at XM (Mo on top of Te) and MX (Te on top of Mo) stackings. At some high symmetry \mathbf{k} points, DFT wave functions for certain bands are localized at the MM (Mo on top of Mo) stacking [39], which are covered by linear combinations of our Wannier functions. The Wannier-interpolated bands, along with the DFT bands, are shown in Fig. 1, where an excellent agreement is observed.

In this work, we mainly employ two indicators to compare band geometry of moiré minibands and LLs, namely the trace of the Fubini-Study metric $\text{tr}(g)$ and the Berry curvature Ω . For LLs, the integration of $\text{tr}(g)$

$$\chi = \frac{1}{2\pi} \int_{\text{BZ}} d\mathbf{k} \text{tr}[g(\mathbf{k})] \quad (1)$$

is $2n + 1$, where n is the LL index. With Wannier functions, our calculated results of χ are 1.04, 3.02, 5.11, 7.53 for the topmost four moiré bands, resembling that of LLs. Another important feature of LLs is that they have flat Ω and $\text{tr}(g)$. Targeting the second moiré valence, we plot the distribution of Ω and $\text{tr}(g)$ in the Brillouin zone in Fig. 2(b,c). The fluctuation of Ω and $\text{tr}(g)$ is relatively large, with the standard deviation being 0.51 and 0.67, respectively (Table I). We will show that electron-electron interactions can improve the flatness of Ω and $\text{tr}(g)$ by band mixing.

Coulomb interaction.—To include the electron-electron interactions, we adopt the following interacting Hamiltonian

$$\hat{H}_{\text{int}} = \sum_{\{n\}, \{\mathbf{k}\}, \mathbf{q}} V_{n_1 n_2 n_3 n_4}(\mathbf{k}_1, \mathbf{k}_2, \mathbf{q}) \hat{a}_{n_1 \mathbf{k}_1}^\dagger \hat{a}_{n_2 \mathbf{k}_2}^\dagger \hat{a}_{n_3 \mathbf{k}_2 - \mathbf{q}} \hat{a}_{n_4 \mathbf{k}_1 + \mathbf{q}},$$

$$V_{n_1 n_2 n_3 n_4}(\mathbf{k}_1, \mathbf{k}_2, \mathbf{q}) = \frac{1}{2A} v(\mathbf{q}) f_{n_1 n_4}(\mathbf{k}_1, \mathbf{q}) f_{n_2 n_3}(\mathbf{k}_2, -\mathbf{q}), \quad (2)$$

where $\hat{a}_{n\mathbf{q}}^\dagger$ creates a Bloch state for band n at crystal momentum \mathbf{q} and A is the area of the system. The summation over \mathbf{k} is in the Brillouin zone and the summation of \mathbf{q} is unbounded. We have taken the convention that the Bloch state is periodic with respect to the reciprocal lattice vectors. We choose the Coulomb interaction screened by symmetric metal gate: $v(\mathbf{q}) = e^2 \tanh(|\mathbf{q}|d) / 2\epsilon_0 \epsilon |\mathbf{q}|$. Here, e is the elementary charge; d is the distance between tMoTe₂ and the metal gate; ϵ is relative permittivity; ϵ_0 is the vacuum permittivity. The form factor $f_{n_1 n_2}(\mathbf{k}, \mathbf{q})$ is defined as

$$f_{n_1 n_2}(\mathbf{k}, \mathbf{q}) = \langle n_1 \mathbf{k} | e^{-i\mathbf{q} \cdot \mathbf{r}} | n_2 \mathbf{k} + \mathbf{q} \rangle, \quad (3)$$

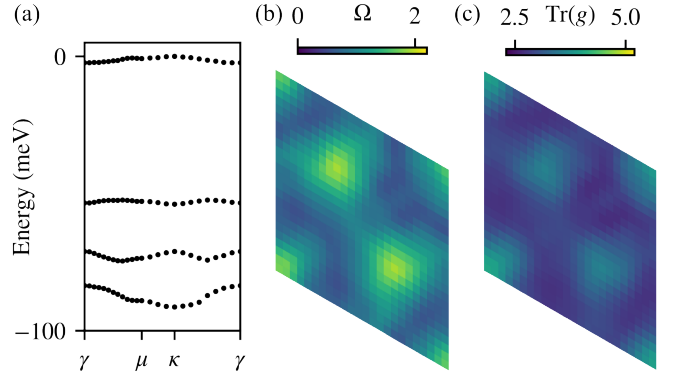


FIG. 3. Hartree-Fock calculations with Wannier functions. (a) shows the Hartree-Fock quasiparticle bands. (b) and (c) show the distribution of the Berry curvature Ω and trace of the Fubini-Study metric tensor $\text{tr}(g)$ in the Brillouin zone for the second moiré miniband after HF calculations. The color scale of (b) and (c) is the same as Fig. 2(b,c).

where $|n, \mathbf{k}\rangle$ is a Bloch state. To compute the form factor, we calculate the matrix element $\langle n_1 \mathbf{R}_1 | e^{-i\mathbf{q} \cdot \mathbf{r}} | n_2 \mathbf{R}_2 \rangle$, where $|n\mathbf{R}\rangle$ is the n th Wannier function sitting at the unit cell labeled by the lattice vector \mathbf{R} . $f_{n_1 n_2}(\mathbf{k}, \mathbf{q})$ can then be obtained by a Fourier transformation.

Signatures of non-Abelian states.—One of the most fascinating features in higher LLs is the non-Abelian state such as the MR state. Moore-Read states can be thought of as superconducting paired CFLs, and is known to be the exact ground state of a pure three-body short ranged interaction in the lowest Landau level [40] or stabilized by the more realistic Coulomb interaction in the first Landau level. To explore whether this non-Abelian state can appear in tMoTe₂ at zero magnetic field, ED calculations are required. However, direct ED calculations at doping $\nu = -5/2$ are prohibitively demanding. Here, we carry out HF calculations at doping $\nu = -2$ (two holes per moiré unit cell) to select the active orbitals.

The central object in HF calculations is the one-body reduced density matrix $\rho_{n_1 n_2}(\mathbf{k}_1, \mathbf{k}_2) = \langle \hat{a}_{n_2 \mathbf{k}_2}^\dagger \hat{a}_{n_1 \mathbf{k}_1} \rangle$. For an arbitrary ρ , a mean field decomposition of \hat{H}_{int} gives rise to the HF interaction Hamiltonian $\hat{H}_{\text{HF}}[\rho]$. In DFT calculations, part of the electron-electron interaction has already been taken into account. To avoid double counting, we subtract the $\hat{H}_{\text{HF}}[\rho_0]$ from the total Hamiltonian:

$$\hat{H} = \sum_{n, \mathbf{k}} \epsilon_{n\mathbf{k}} \hat{a}_{n\mathbf{k}}^\dagger \hat{a}_{n\mathbf{k}} + \hat{H}_{\text{int}} - \hat{H}_{\text{HF}}[\rho_0]. \quad (4)$$

Here, $\epsilon_{n\mathbf{k}}$ is the DFT band energy, and ρ_0 is the one-body reduced density matrix from the DFT calculations. HF calculations are carried out with \hat{H} defined above. The subtraction of $\hat{H}_{\text{HF}}[\rho_0]$ ensures that when all valence bands are occupied, the HF calculations reproduce exactly the same band energies and Bloch states from DFT calculations.

The results of Hartree-Fock calculations are presented in Fig. 3. Only frozen bands are included in the calculations.

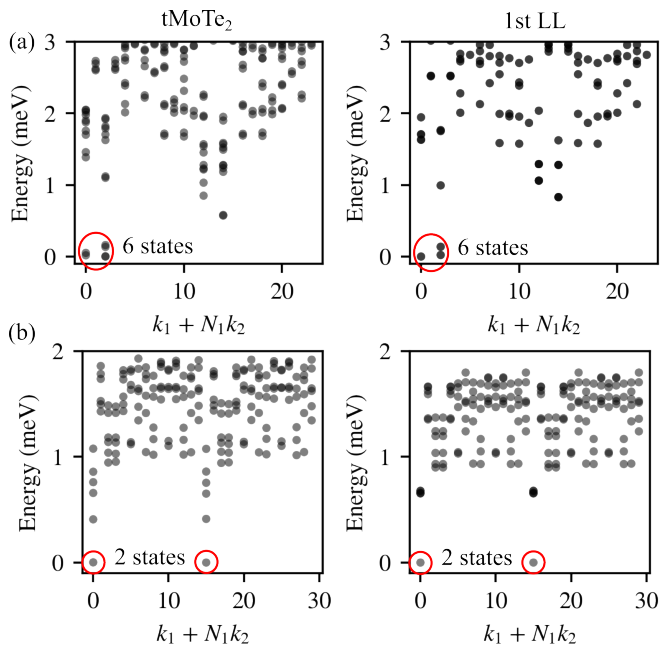


FIG. 4. Many-body spectrum of tMoTe₂ with twist angle 2° and LL on a 4 × 6 [(a)] and 5 × 6 [(b)] supercell with periodic boundary condition. The horizontal axis is the total momentum of all electrons. For LL, unscreened Coulomb interaction is used. Parameters: $\epsilon = 5$, $d = 300$ Å.

An enhanced gap between the first and second moiré valence bands can be observed. Crucially, after HF calculations, the fluctuations of Ω and $\text{tr}(g)$ are significantly reduced by approximately 50% (Table I), while χ slightly improves (3.09 to 3.02). The improvement of band geometry enhances the analogy between the second moiré band and the first LL.

Focusing on the second moiré valence band, we carry out ED calculations on top of the HF calculations. To avoid double counting of electron-electron interaction, we again utilize Eq. (4) as the Hamiltonian in ED calculations. In this context, ϵ_{nk} and ρ_0 in Eq. (4) are band energies and one-body reduced density matrix from HF calculations. Previously, the double counting removing procedure for HF calculations on top of DFT calculations is heuristic. However, the same procedure, used for ED calculations on top of HF calculations, is exact. The sole purpose of HF calculations is to select relevant Bloch states as single particle orbitals for ED calculations.

On a 4 × 3 supercell with periodic boundary condition, our ED calculations, restricted to the second moiré valence bands from both valleys, show that fully valley polarized state is the ground state with parameters specified in the caption of Fig. 4. Therefore, we further restrict the ED calculations to the second moiré valence band from the K valley. The many-body spectrums are shown in Fig. 4 for 4 × 6 and 5 × 6 supercells with periodic boundary condition. The six-fold and two-fold ground state degeneracy with even and odd number of electrons is the hallmark of

TABLE I. Many-body gaps of non-Abelian state for tMoTe₂ and relevant band geometry properties, including the integration of the quantum metric (χ), the standard deviation of the Berry curvature ($\Delta\Omega$) and the quantum metric [$\Delta\text{tr}(g)$], at various twist angles (θ). NaN indicates that no evidence of non-Abelian states has been found. The gap is identified on a 4 × 6 supercell and the parameters are the same as that specified in the caption of Fig. 4.

θ	Before HF			After HF			Gap
	χ	$\Delta\Omega$	$\Delta\text{tr}(g)$	χ	$\Delta\Omega$	$\Delta\text{tr}(g)$	
1.89°	3.07	0.88	0.79	3.04	0.72	0.59	NaN
2.00°	3.09	0.51	0.67	3.02	0.32	0.27	0.41
2.14°	3.15	0.99	1.08	3.06	0.28	0.27	0.11

the non-Abelian states of MR type or its particle hole conjugate. In Fig. 4, we also show the many-body spectrum of half-filled first Landau level with Coulomb interaction $v(\mathbf{q}) = e^2/2\epsilon_0\epsilon|\mathbf{q}|$. The Landau level system is put on a triangular lattice with the same lattice constant as tMoTe₂ at twist angle 2°. The striking similarity of the many-body spectrum between tMoTe₂ and the LL system is another strong indication of the non-Abelian states.

In the Supplemental Material, we present the many-body spectrum on a 4 × 6 supercell of half-filled tMoTe₂ second valence band, but with bare DFT bands. The spectrum bears similarity to that of the half-filled first LL, but lacks the six-fold ground state degeneracy. Therefore, the improved band geometry from HF calculations is crucial for the non-Abelian states to appear.

We have also performed calculations for twist angles 1.89° and 2.14°. The band geometry before and after HF calculations is presented in Table I. Evidence of non-Abelian states is also found at twist angle 2.14°, but with a smaller many-body gap. No non-Abelian states are found at 1.89°, for which the fluctuations of Ω and $\text{tr}(g)$ are not significantly suppressed by HF calculations.

In LL systems, the Moore-Read (Pfaffian) state and its particle-hole (PH) conjugate anti-Pfaffian state are degenerate if LL mixing effects were ignored; the LL mixing provides a PH breaking effect and selects anti-Pfaffian over Pfaffian [41]. Besides Pfaffian and anti-Pfaffian, an intrinsically PH symmetric topological order, PH-Pfaffian, was also proposed [42?]. In our systems, the PH symmetry is explicitly broken by the dispersion and non-uniform quantum geometries. We leave more detailed examination of the precise nature of our ground state to the future work, which can be addressed by wave function overlap and entanglement spectrum analysis.

Compared to Laughlin states and other Jain sequence states, signatures of non-Abelian states presented here are much weaker. It has been shown that the $\nu = -2/3$ Laughlin state exists in a wide range of twist angles in tMoTe₂ [7]. However, evidences of non-Abelian states are only found at two commensurate twist angles in this work. In addition, the many-body gap in Fig. 4 is also several times smaller

than that of the $\nu = -2/3$ Laughlin state at the same interaction strength. Finally, our choice of the dielectric constant ϵ gives rise to characteristic interaction strength that is several times larger than the band gap. Therefore, it should be critically evaluated whether the non-Abelian state is stable against band mixing in $t\text{MoTe}_2$, which was proved to be crucial in understanding Laughlin states in the same system at twist angle around 3.89° [43–45].

We acknowledge useful discussions with Yuchi He, Ying Ran, Lingnan Shen, and Kai Sun. The exact diagonalization study is supported by DOE Award No. DE-SC0012509. The density-functional theory calculation is supported by the Center on Programmable Quantum Materials, an Energy Frontier Research Center funded by DOE BES under award DE-SC0019443. The machine learning of moiré structure is supported by the discovering AI@UW Initiative and by the National Science Foundation under Award DMR-2308979. This work uses Microsoft Azure credits funded by discovering AI@UW Initiative.

Note added.— We recently became aware of Refs. [46–48]. Ref. [46] proposed the existence of non-Abelian states in free electron gas coupled to Skyrmion lattices. An updated version of Ref. [46] and Refs. [47 and 48] proposed the existence of non-Abelian states in $t\text{MoTe}_2$ based on continuum models fitted to DFT bands.

* These authors contribute equally to the work.

† tingcao@uw.edu

* dixiao@uw.edu

- [1] J. Cai, E. Anderson, C. Wang, X. Zhang, X. Liu, W. Holtzmann, Y. Zhang, F. Fan, T. Taniguchi, K. Watanabe, *et al.*, Signatures of fractional quantum anomalous Hall states in twisted MoTe_2 , *Nature* **622**, 63 (2023).
- [2] H. Park, J. Cai, E. Anderson, Y. Zhang, J. Zhu, X. Liu, C. Wang, W. Holtzmann, C. Hu, Z. Liu, *et al.*, Observation of fractionally quantized anomalous Hall effect, *Nature* **622**, 74 (2023).
- [3] Y. Zeng, Z. Xia, K. Kang, J. Zhu, P. Knüppel, C. Vaswani, K. Watanabe, T. Taniguchi, K. F. Mak, and J. Shan, Thermodynamic evidence of fractional Chern insulator in moiré MoTe_2 , *Nature* **622**, 69 (2023).
- [4] F. Xu, Z. Sun, T. Jia, C. Liu, C. Xu, C. Li, Y. Gu, K. Watanabe, T. Taniguchi, B. Tong, J. Jia, Z. Shi, S. Jiang, Y. Zhang, X. Liu, and T. Li, Observation of integer and fractional quantum anomalous Hall effects in twisted bilayer MoTe_2 , *Phys. Rev. X* **13**, 031037 (2023).
- [5] Z. Lu, T. Han, Y. Yao, A. P. Reddy, J. Yang, J. Seo, K. Watanabe, T. Taniguchi, L. Fu, and L. Ju, Fractional quantum anomalous Hall effect in multilayer graphene, *Nature* **626**, 759 (2024).
- [6] H. Li, U. Kumar, K. Sun, and S.-Z. Lin, Spontaneous fractional Chern insulators in transition metal dichalcogenide moiré superlattices, *Phys. Rev. Res.* **3**, L032070 (2021).
- [7] C. Wang, X.-W. Zhang, X. Liu, Y. He, X. Xu, Y. Ran, T. Cao, and D. Xiao, Fractional Chern insulator in twisted bilayer mote_2 , *Phys. Rev. Lett.* **132**, 036501 (2024).
- [8] A. P. Reddy, F. Alsallom, Y. Zhang, T. Devakul, and L. Fu, Fractional quantum anomalous Hall states in twisted bilayer MoTe_2 and WSe_2 , *Phys. Rev. B* **108**, 085117 (2023).
- [9] V. Crépel and L. Fu, Anomalous hall metal and fractional Chern insulator in twisted transition metal dichalcogenides, *Phys. Rev. B* **107**, L201109 (2023).
- [10] N. Morales-Durán, J. Wang, G. R. Schleder, M. Angeli, Z. Zhu, E. Kaxiras, C. Repellin, and J. Cano, Pressure-enhanced fractional Chern insulators along a magic line in moiré transition metal dichalcogenides, *Phys. Rev. Res.* **5**, L032022 (2023).
- [11] J. Dong, J. Wang, P. J. Ledwith, A. Vishwanath, and D. E. Parker, Composite fermi liquid at zero magnetic field in twisted mote_2 , *Phys. Rev. Lett.* **131**, 136502 (2023).
- [12] H. Goldman, A. P. Reddy, N. Paul, and L. Fu, Zero-field composite fermi liquid in twisted semiconductor bilayers, *Phys. Rev. Lett.* **131**, 136501 (2023).
- [13] T. Neupert, L. Santos, C. Chamon, and C. Mudry, Fractional Quantum Hall States at Zero Magnetic Field, *Phys. Rev. Lett.* **106**, 236804 (2011).
- [14] E. Tang, J.-W. Mei, and X.-G. Wen, High-Temperature Fractional Quantum Hall States, *Phys. Rev. Lett.* **106**, 236802 (2011).
- [15] D. Sheng, Z.-C. Gu, K. Sun, and L. Sheng, Fractional quantum Hall effect in the absence of Landau levels, *Nat. Commun.* **2**, 389 (2011).
- [16] N. Regnault and B. A. Bernevig, Fractional Chern Insulator, *Phys. Rev. X* **1**, 021014 (2011).
- [17] F. Wu, T. Lovorn, E. Tutuc, I. Martin, and A. MacDonald, Topological Insulators in Twisted Transition Metal Dichalcogenide Homobilayers, *Phys. Rev. Lett.* **122**, 086402 (2019).
- [18] H. Yu, M. Chen, and W. Yao, Giant magnetic field from moiré induced Berry phase in homobilayer semiconductors, *Natl. Sci. Rev.* **7**, 12 (2020).
- [19] S. A. Parameswaran, R. Roy, and S. L. Sondhi, Fractional Chern insulators and the W_∞ algebra, *Phys. Rev. B* **85**, 241308 (2012).
- [20] R. Roy, Band geometry of fractional topological insulators, *Phys. Rev. B* **90**, 165139 (2014).
- [21] B. Mera and T. Ozawa, Kähler geometry and Chern insulators: Relations between topology and the quantum metric, *Phys. Rev. B* **104**, 045104 (2021).
- [22] T. Ozawa and B. Mera, Relations between topology and the quantum metric for Chern insulators, *Phys. Rev. B* **104**, 045103 (2021).
- [23] J. Wang, J. Cano, A. J. Millis, Z. Liu, and B. Yang, Exact Landau level description of geometry and interaction in a flatband, *Phys. Rev. Lett.* **127**, 246403 (2021).
- [24] P. J. Ledwith, A. Vishwanath, and D. E. Parker, Vortexability: A unifying criterion for ideal fractional Chern insulators, *arXiv:2209.15023* (2022).
- [25] J. Wang, S. Klevtsov, and Z. Liu, Origin of model fractional Chern insulators in all topological ideal flatbands: Explicit color-entangled wave function and exact density algebra, *Phys. Rev. Res.* **5**, 023167 (2023).
- [26] M. Fujimoto, D. E. Parker, J. Dong, E. Khalaf, A. Vishwanath, and P. Ledwith, Higher vortexability: zero field realization of higher Landau levels, *arXiv:2403.00856* (2024).
- [27] G. Moore and N. Read, Nonabelions in the fractional quantum Hall effect, *Nucl. Phys. B* **360**, 362 (1991).
- [28] R. Willett, J. P. Eisenstein, H. L. Störmer, D. C. Tsui, A. C. Gossard, and J. H. English, Observation of an even-denominator quantum number in the fractional quantum Hall effect, *Phys. Rev. Lett.* **59**, 1776 (1987).
- [29] M. Storni, R. H. Morf, and S. Das Sarma, Fractional quantum

- Hall state at $\nu = \frac{5}{2}$ and the Moore-Read Pfaffian, Phys. Rev. Lett. **104**, 076803 (2010).
- [30] P. Bonderson, A. Kitaev, and K. Shtengel, Detecting non-abelian statistics in the $\nu = 5/2$ fractional quantum Hall state, Phys. Rev. Lett. **96**, 016803 (2006).
- [31] A. Wójs, G. Möller, S. H. Simon, and N. R. Cooper, Skyrmions in the Moore-Read state at $\nu = \frac{5}{2}$, Phys. Rev. Lett. **104**, 086801 (2010).
- [32] X.-W. Zhang, C. Wang, X. Liu, Y. Fan, T. Cao, and D. Xiao, Polarization-driven band topology evolution in twisted MoTe₂ and WSe₂, arXiv:2311.12776 (2023).
- [33] K. Kang, B. Shen, Y. Qiu, Y. Zeng, Z. Xia, K. Watanabe, T. Taniguchi, J. Shan, and K. F. Mak, Evidence of the fractional quantum spin Hall effect in moiré MoTe₂, Nature (2024).
- [34] J. D. Cloizeaux, Energy bands and projection operators in a crystal: Analytic and asymptotic properties, Phys. Rev. **135**, A685 (1964).
- [35] N. Marzari and D. Vanderbilt, Maximally localized generalized Wannier functions for composite energy bands, Phys. Rev. B **56**, 12847 (1997).
- [36] N. Marzari, A. A. Mostofi, J. R. Yates, I. Souza, and D. Vanderbilt, Maximally localized Wannier functions: Theory and applications, Rev. Mod. Phys. **84**, 1419 (2012).
- [37] I. Souza, N. Marzari, and D. Vanderbilt, Maximally localized Wannier functions for entangled energy bands, Phys. Rev. B **65**, 035109 (2001).
- [38] C. Brouder, G. Panati, M. Calandra, C. Mourougane, and N. Marzari, Exponential localization of Wannier functions in insulators, Phys. Rev. Lett. **98**, 046402 (2007).
- [39] W.-X. Qiu, B. Li, X.-J. Luo, and F. Wu, Interaction-driven topological phase diagram of twisted bilayer MoTe₂, Phys. Rev. X **13**, 041026 (2023).
- [40] L. Zhang and X.-Y. Song, Moore-read state in half-filled moiré Chern band from three-body pseudo-potential, arXiv:2403.11478 (2024).
- [41] E. H. Rezayi, Landau level mixing and the ground state of the $\nu = 5/2$ quantum Hall effect, Phys. Rev. Lett. **119**, 026801 (2017).
- [42] D. T. Son, Is the composite fermion a Dirac particle?, Phys. Rev. X **5**, 031027 (2015).
- [43] J. Yu, J. Herzog-Arbeitman, M. Wang, O. Vafek, B. A. Bernevig, and N. Regnault, Fractional Chern insulators versus nonmagnetic states in twisted bilayer MoTe₂, Phys. Rev. B **109**, 045147 (2024).
- [44] C. Xu, J. Li, Y. Xu, Z. Bi, and Y. Zhang, Maximally localized wannier functions, interaction models, and fractional quantum anomalous Hall effect in twisted bilayer MoTe₂, Proc. Natl. Acad. Sci. U.S.A. **121**, e2316749121 (2024).
- [45] A. Abouelkomsan, A. P. Reddy, L. Fu, and E. J. Bergholtz, Band mixing in the quantum anomalous Hall regime of twisted semiconductor bilayers, Physical Review B **109**, L121107 (2024).
- [46] A. P. Reddy, N. Paul, A. Abouelkomsan, and L. Fu, Non-Abelian fractionalization in topological minibands, arXiv:2403.00059 (2024).
- [47] C. Xu, N. Mao, T. Zeng, and Y. Zhang, Multiple Chern bands in twisted MoTe₂ and possible non-Abelian states, arXiv:2403.17003 (2024).
- [48] C.-E. Ahn, W. Lee, K. Yananose, Y. Kim, and G. Y. Cho, First landau level physics in second moiré band of 2.1° twisted bilayer MoTe₂, arXiv:2403.19155 (2024).